American Mineralogist, Volume 84, pages 1766–1780, 1999

Textural development of monazite during high-grade metamorphism: Hydrothermal growth kinetics, with implications for U,Th-Pb geochronology

JOHN C. AYERS,* CALVIN MILLER, BETSY GORISCH, AND JOHN MILLEMAN

Department of Geology, Vanderbilt University, Nashville, Tennessee 37235, U.S.A.

ABSTRACT

Monazite has become an important tool for geochronology, but it commonly exhibits complex internal zoning of composition and age. Experiments were conducted to characterize the textural development and the rate and mechanism of growth of finely powdered (<3 μm) natural monazite in quartzite ± H_2O at 1.0 GPa and 1000 °C. Coarsely crushed quartz crystals <1 to >500 μm in diameter grew rapidly and progressively engulfed monazite crystals to form arrays of monazite inclusions. The mean diameter of all monazite crystals decreased in the first 24 h, then increased at a constant rate consistent with growth by grain boundary diffusion-controlled Ostwald ripening with a minimum rate constant $K_{1/4} = 4.41 \times 10^{-2}$ μm/s^4. Using small quartz crystals of uniform diameter (~0.5 μm) in the starting material reduced quartz grain boundary mobility and limited the development of inclusions. Monazite grew by matrix volume diffusion-controlled Ostwald ripening with $K_{1/3} = 1.02 \times 10^{-2}$ μm/s^3. In all run products, matrix coarsening produced linear crystal-size distributions that reflect continuous recrystallization and nucleation. Textural evidence suggests that matrix coarsening-induced coalescence was also an important growth mechanism.

During annealing of fluid-filled rock, growing host crystals may occlude small monazite crystals, preserving their isotopic composition. Large monazite crystals may pin grain boundaries, while smaller crystals may move with grain boundaries by recrystallizing, a process that resets isotopic systems. Monazite crystals on grain boundaries may grow by Ostwald ripening to form rims and by coalescence. Accurate interpretations of monazite ages therefore require knowledge of the texture/growth history of the rock and its dated grains.

INTRODUCTION

Monazite grains commonly contain multiple growth zones of different age. To interpret correctly the significance of measured zone ages, we need to know what causes monazite to grow. In this paper, we examine monazite paragenesis, identify zoning types in natural monazite grains, and propose growth mechanisms that account for their geometry. We then attempt to characterize the simplest growth mechanism, coarsening in a hydrostatic closed system, by presenting results of monazite growth experiments in quartzite ± H_2O at 1.0 GPa and 1000 °C. We use crystal-size distribution (CSD) values measured as a function of time to estimate the rate of growth and identify the growth mechanism. We also investigate the effect of matrix coarsening on monazite growth rate and mechanism, and in the process obtain insights into inclusion/host relations.

Monazite paragenesis

Monazite commonly occurs as an accessory phase in peraluminous granites and amphibolite- and granulite-grade metapelites. It is, however, uncommon during diagenesis and low-grade metamorphism of shales, an observation that some attribute to instability at these conditions (Overstreet 1967; Sawka et al. 1986), although U,Th-Pb studies have identified (metastable?) detrital monazite in high-grade metapelites (Parrish 1990; Suzuki et al. 1994).

During prograde metamorphism, monazite may grow at staurolite grade conditions (~500 °C) through heterogeneous reaction involving apatite and LREE oxides (Kingsbury et al. 1993; Akers et al. 1993) or by breakdown of allanite (Smith and Barreiro 1990). Bingen and van Breeman (1998) document prograde growth of monazite by breakdown of hydrous minerals including allanite, biotite, and hornblende. The reconnaissance of textures by Kingsbury et al. (1993) suggest that monazite mean crystal size increases with increasing metamorphic grade, and the distribution of crystal size shows a subtle shift from lognormal to normal distributions. This is consistent with the observations and predictions of Cashman and Ferry (1988) that initial nucleation produces a lognormal distribution (as observed in contact metamorphic rocks) and that subsequent coarsening removes the small grains and changes the distribution to normal (as observed in rocks that experienced prolonged regional metamorphism). Coarsening reduces the surface area/volume ratio by growing large, spherical grains at the expense of smaller grains, and spherical shape is often used as evidence of metamorphic growth (e.g., Heaman and Parrish 1991). Kingsbury et al. (1993) also observed an increase in the fraction of monazite grains present as inclusions with increasing metamorphic grade. This is consistent with the field-based observation of Bea (1996) that >70% of the mass

---

*E-mail: john.c.ayers@vanderbilt.edu

0003-004X/99/1112–1766$05.00

fraction of monazite (and zircon) in granitoids and granulites is present as inclusions.

Recent studies have shown that monazite may grow or recrystallize not only during prograde and peak metamorphism, but also during retrograde metamorphism. Lanzirotti and Hanson (1996) describe a sheared sample in which monazites yielded concordant ages that they interpreted to represent the time of retrograde growth. Shear strain and fluid probably both contributed to the recrystallization of monazite in these rocks. Fitzsimmons et al. (1997) described monazites from an anatectic leucogneiss that have low-Th magmatic cores with oscillatory zoning and high-Th rims that appear distinctly brighter in backscattered electron images. Both yield concordant U-Pb ages with mean values of 528 ± 4 Ma for cores and 518 ± 3 Ma for rims. They attribute the late monazite growth to retrograde hydrous fluids exsolved from late-stage crystallizing silicate melts. The same processes may be responsible for a 26 Ma spread of concordant U-Pb monazite ages following crystallization of a granite dike observed by Hawkins and Bowring (1997).

Little is known about heterogeneous peak and retrograde reactions that produce monazite. Pan (1997), however, identified monazite- and zircon-forming reactions involving other accessory minerals (rutile and titanite) that participate in other well-calibrated heterogeneous reactions, allowing him to correlate monazite and zircon U-Pb ages with thermobarometric estimates. Because multiple generations of monazite and zircon formed at different times, he could identify a series of *P-T-t* points and thus characterize the shape and position of the peak and retrograde *P-T-t* path.

The study by Pan (1997) illustrates the power of dating multiple growth zones in monazite, given an understanding of monazite growth mechanisms. Monazite may grow in a variety of ways, including homogeneous reaction caused by (1) recrystallization and coarsening, possibly in presence of fluid or melt, or (2) intersection of a solvus during cooling (e.g., the monazite-huttonite solvus; see Gratz and Heinrich 1997); or heterogeneous reaction during (3) prograde, (4) peak, or (5) retrograde metamorphism. Evidence presented above suggests that mechanism (1) occurs commonly during peak and retrograde metamorphism to form recrystallized monazite with distinctly different composition from preexisting monazite. Recrystallization also causes total or partial resetting of the U,Th-Pb system and overprinting of preexisting zoning with new zoning features (Fig. 1). This paper attempts to characterize mechanism (1), growth of monazite by coarsening, i.e., recrystallization in closed systems by homogeneous reaction in the absence of shear strain.

Monazite zoning: Clues to identifying growth mechanisms

Monazite exhibits several complex types of zoning evident in backscattered electron (BSE) images (Fig. 1). Growth zones are distinguished by variations in Th concentration primarily resulting from substitution of huttonite ($ThSiO_4$) and brabantite [$CaTh(PO_4)_2$] for monazite REE(PO_4) (Fitsimmons et al. 1997). Zoning types in monazite include fine-scale oscillatory zoning resulting from igneous growth (Fig. 1a); concentric or quasi-concentric zoning in which locally thick, homogeneous concentric zones alternate or show discrete, directional change in composition; veining (Fig. 1b); irregular rims (Fig. 1d); and exsolution lamellae (rare, see Fig. 1b of Parrish 1990). Some types of zones appear to represent in-situ hydrothermal alteration that changes the composition of the monazite and resets the U,Th-Pb system. For example, we and others have observed a style of zoning that we call "patchy zoning," characterized by irregularly shaped, subequant zones with distinct backscattered intensity (composition) associated with embayments, fractures, and inclusions (Fig. 1c). The patchy zones texturally appear to overprint preexisting zoning. We have observed patchy zoning in monazite from peraluminous granite (the Ireteba pluton, Fig. 1c, Miller et al. 1997) and from granulite-grade metamorphic rocks (Winding Stair Gap in the Appalachian Blue Ridge, Miller et al. 1996). Hawkins and Bowring (1997) and Poitrasson et al. (1996) also observed patchy zoning in monazite from granitoids. By dating single crystal fragments using thermal-ionization mass spectrometry (TIMS), Hawkins and Bowring (1997) found that patchy zones yield concordant ages younger than unaltered monazite. Likewise, our ion microprobe (IMP) studies of the Ireteba granite show that patchy alteration zones yield younger ages than the unaltered zones (Fig. 1d; Miller et al. 1997; Townsend et al. 1998). Poitrasson et al. (1996) suggested that alteration progresses from margin to core and along fractures, and results in depletion of the rare-earth elements (REE, especially light REE) and enrichment of Th. They surmised that changes in composition resulted from selective leaching rather than addition. Taken *in toto*, this evidence suggests that patchy zoning results from recrystallization during in-situ hydrothermal alteration of preexisting monazite (Poitrasson et al. 1996; Hawkins and Bowring 1997).

In-situ monazite recrystallization may also result from coarsening of matrix minerals during prolonged annealing at high *T*. Generally, grain boundaries of matrix minerals migrate toward their center of curvature, resulting in the shrinkage and disappearance of small crystals and coarsening of larger crystals. The most energetically favorable textural position of accessory minerals is on grain boundaries (Watson et al. 1989), so when those grain boundaries move, accessory mineral crystals will tend to move with them by recrystallizing through a dissolution-reprecipitation process. In keeping with this prediction, Getty and Gromet (1992) attributed partial resetting of the monazite U-Pb system in the Willimantic dome to monazite recrystallization during deformation and matrix coarsening of pelitic gneisses.

In closed systems, monazite may recrystallize by Ostwald ripening, a process in which large crystals of a dispersed phase (an accessory mineral) grow young, chemically homogeneous rims at the expense of more soluble smaller crystals through simultaneous dissolution and precipitation. The driving force for ripening, minimization of the surface free energy by reduction of total surface area/volume, results in the production of rounded crystals because the sphere has the lowest surface area per unit volume of any shape. The process of dissolution of small monazite crystals, transport, and precipitation of young monazite rims on older cores results in a partial recrystallization of monazite in a rock, changing the crystal-size distribution and partially resetting the monazite U, Th-Pb system.

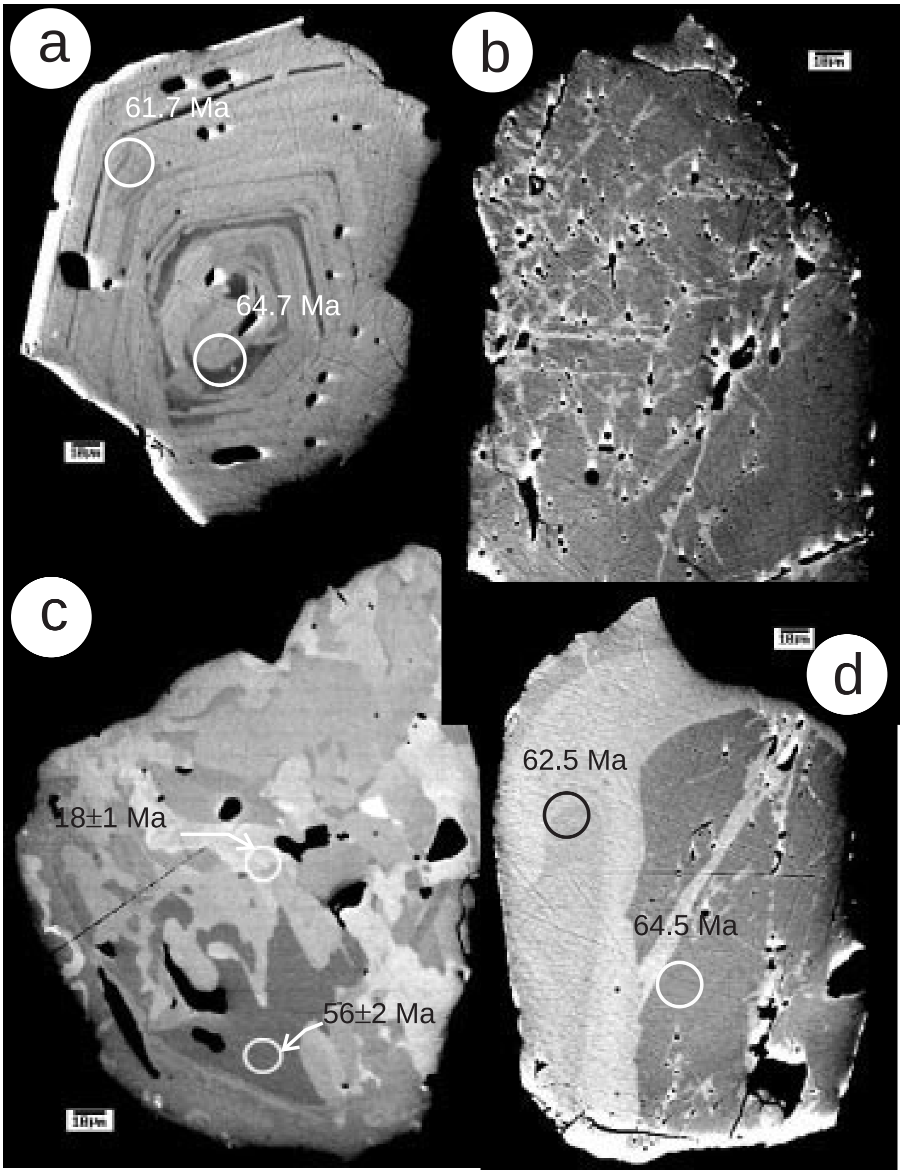

FIGURE 1. BSE images of monazite crystals illustrating zoning types. (**a**) From White Rock Wash granite in southern Nevada, showing concentric zoning. (**b**) From Ireteba granite in southern Nevada, showing veining. (**c**) From Ireteba granite in southern Nevada, showing patchy zoning. (**d**) From Ireteba granite in southern Nevada, showing irregular overgrown rim and veining. Ion microprobe analysis spots and measured ages in millions of years (Ma) shown.

Crystal-size distributions: Clues to identifying growth mechanism and rate

During Ostwald ripening, crystals with radii less than a critical radius r^* (generally equal to the mean radius, see Joesten 1991) will shrink, while crystals with $r > r^*$ will grow. The value of r^* increases with time, so that some crystals may grow early but then shrink when r^* exceeds their radii ($r < r^*$). Once a population of crystals reaches textural equilibrium, the crystal-size frequency vs. r/r^* curve assumes a characteristic shape described by Lefshitz, Slyozov, and Wagner (LSW) theory (Joesten 1991; Rahaman 1995, Lefshitz and Slyozov 1961; Wagner 1961).

The distribution of crystal sizes in a rock provides information on the duration and mechanism of crystal growth. Crystal-size frequency histograms, the shapes of which depend on the relative rates of nucleation and coarsening and the duration of annealing, summarize the distribution of measured values of crystal length (diameter) L (e.g., Figs. 2–4). If annealing time is short and nucleation rate is high, the distribution is lognormal. Conversely, long annealing times result in the dissolution of crystals below the critical radius r^* and growth of crystals larger than r^*, resulting in a normal distribution (Cashman and Ferry 1988).

Crystal-size distribution (CSD) plots, first applied to metamorphic rocks by Cashman and Ferry (1988), are based on the observation that distributions of crystal sizes measured in three dimensions are usually lognormal (details below). CSD plots can be used to estimate nucleation density and the duration of annealing, given the value of the linear growth rate.

Piston cylinder experiments have been performed at 1.0 GPa and 1000 °C to monitor the temporal evolution of histograms and CSD values of monazite in quartzite ± H_2O. Given the duration of annealing, we use CSD values to estimate the value of the linear growth rate.

EXPERIMENTAL PROCEDURES

Starting materials

In FQMZ (fine quartz and monazite) experiments, we attempted to produce a powder containing optically clear quartz crystals with a uniform size of ~5 μm. We ground quartz to a fine powder, collected crystals <53 μm by passing the powder through a sieve, and placed these crystals in a settling column for 79 minutes. According to Stokes Law, 5 μm crystals should settle 10 cm in this time, so we pipetted the suspension from 10 cm below the water surface, dried, and collected the crystals. A sample of powdered starting material was mounted in epoxy and polished for measurement of crystal size (a description of the measurement procedures to come). As shown in Fig. 2a, the mean quartz size in FQMZ starting material is actually 0.45 ± 0.02 μm (95% confidence limits), with a maximum diameter of 3.6 μm and a variance of 0.22 μm^2. For MG (monazite growth) series experiments we produced a quartz powder with a wide range of crystal size to investigate the effect of matrix coarsening. Quartz coarsely crushed in a mortar and pestle had a mean diameter of 2.7 ± 0.3 μm with a variance of 10.1 μm^2 . Quartz crystals in MG and FQMZ starting materials are sharply angular and many contain multiple fractures.

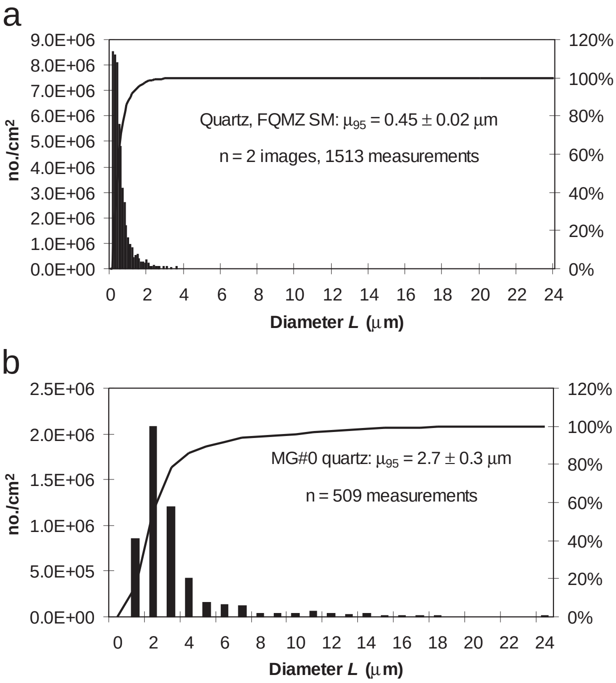

FIGURE 2. Crystal-size frequency histograms (N_A vs. L) of quartz in starting materials: (**a**) FQMZ and (**b**) MG. Both plots use the same scale for L, illustrating that quartz in FQMZ SM is smaller and has a much narrower distribution of sizes than quartz in MG no. 0. Cumulative frequency N^*_A also plotted in percent (right-hand scale).

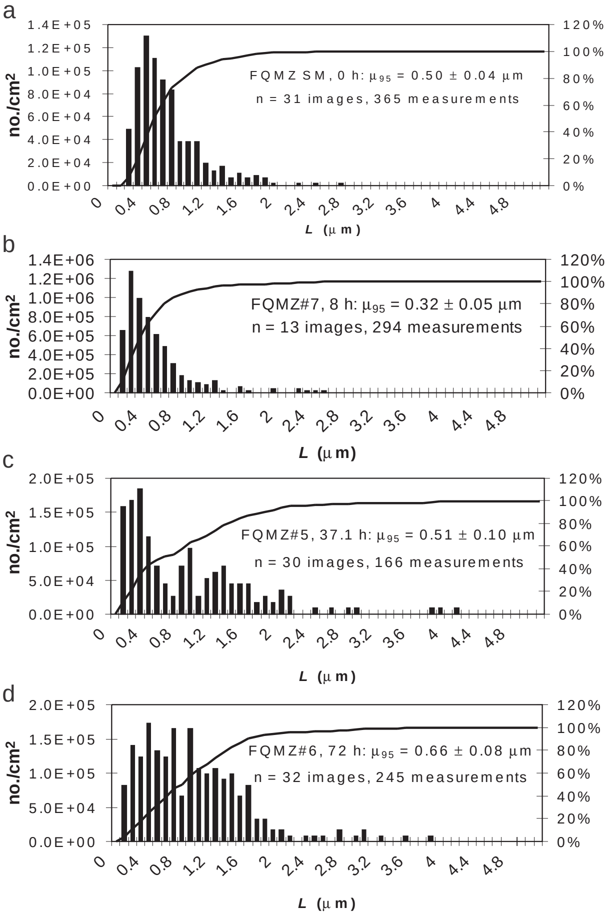

FIGURE 3. Crystal-size frequency histograms of number of crystals per unit area (N_A, vertical bars) and cumulative number of crystals per unit area (N_A*, solid line) vs. diameter L of monazite in FQMZ starting material and run products.

Monazite from Raade, Norway (composition in Rapp and Watson 1986) was ground under ethanol in a mortar and pestle for >10 h and then settled in a water column. Crystals still in suspension after 20 h were collected and found to be predominantly <2 μm in diameter. Combining 2 wt% of this monazite powder with 98 wt% quartz produced the final starting materials. Monazite has a mean crystal diameter of 0.50 ± 0.04 μm in FQMZ (Fig. 3a) and 0.89 ± 0.07 μm in MG starting material (Fig. 4a). Because monazite is roughly twice as dense as quartz (~5.15 vs. 2.65 g/cm^3, see Deer et al. 1966), the volume fraction of monazite in anhydrous experiments is 1.04%, and in experiments with 2 wt% H_2O added, 0.99%.

Piston cylinder experiments

Cold-sealing capsules of the type described by Ayers et al. (1992) were used to encapsulate samples. We fired a Ni capsule (4.4 mm I.D., 6.35 mm O.D., 9–10 mm length) in air for

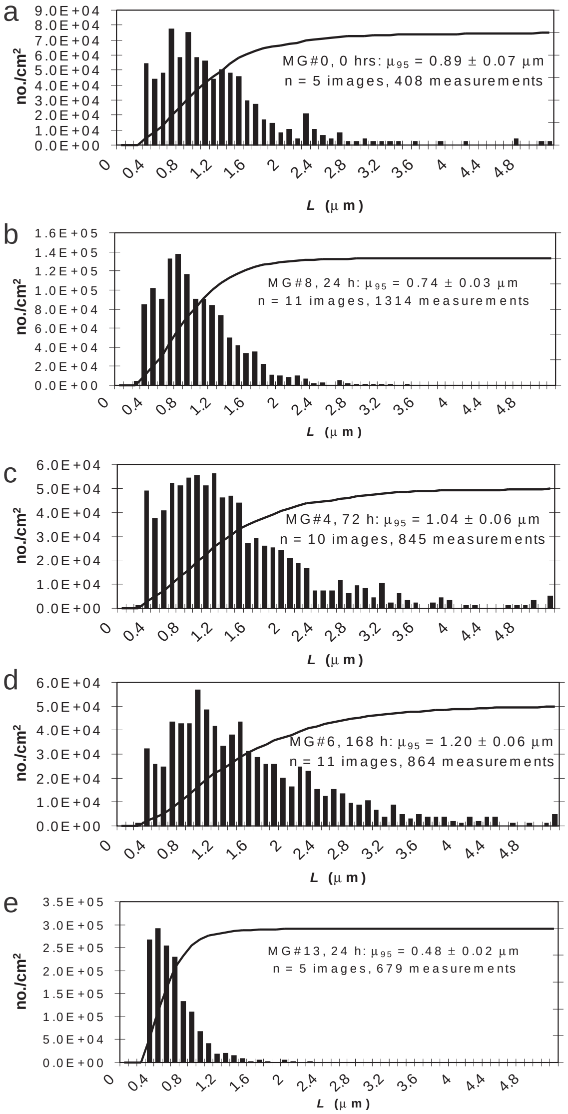

FIGURE 4. Crystal-size frequency histograms of number of crystals per unit area (N_A, vertical bars) and cumulative number of crystals per unit area (N_A*, solid line) vs. diameter *L* of monazite in MG starting material and run products.

12 h at 1000 °C to form a surface layer of NiO that prevented Ni-Pt interdiffusion, and then tapped in a Pt insert (4.4 mm O.D., tri-crimped and welded shut on one end).

After weighing the capsule, we added ~100 mg of powdered starting material to the capsule, weighed the filled capsule to find the weight of starting material, and then added 1–2 wt% H_2O with a microsyringe. We estimate that each sample placed in a capsule contained more than 1 billion monazite crystals. Sampling statistics suggest that samples taken from our starting material should be unbiased and therefore representative. A Pt lid topped by a Ni lid was placed on top and cold-sealed to the capsule by pressurizing in a 1.91 cm piston-cylinder apparatus (Ayers et al. 1992). We conducted all experiments using the assembly and corresponding pressure calibration described by Ayers et al. (1992). A W Re_3/W Re_{25} thermocouple and temperature controller maintained *T* within ± 5 °C of the setpoint, while we manually maintained *P* within ± 500 bars. The thermocouple was calibrated by its manufacturer (Engelhardt) and is accurate to ± 1.5 °C. Table 1 lists all experiment conditions.

Upon completion of each experiment, we sectioned the capsule lengthwise to maximize observable surface area, mounted the sections in and impregnated their surfaces with epoxy, and polished each to 0.06 µm. Energy dispersive analysis and identification in optical grain mount of selected samples showed that monazite and quartz were the only minerals present in our starting materials and run products.

Image analysis methods

We coated sample mounts with a carbon film and then imaged in BSE mode with a scanning electron microscope (SEM). For the MG series run products, we used an ETEC SEM with an accelerating potential of 20 keV, and converted Polaroid photos taken at 1000× to digital format using a scanner. FQMZ run products were imaged on a Hitachi S-4200 SEM at 2000–4000× with an accelerating voltage of 10 keV. We collected 5–10 non-overlapping images for MG experiments and 20–35 images for FQMZ experiments.

Crystal size was measured from 300 dpi, 256 gray-scale level, 3.5 in. × 4 in. digital BSE images using computer-automated image analysis. The spatial resolution was ~0.11 µm at 1000× and 0.028 µm at 4000×. We applied a median filter to reduce electronic noise without affecting the size of features, and then calibrated the spatial scale using a scalebar in the image. To measure monazite crystal size, we thresholded (segmented) the image by classifying each pixel with grayscale level greater than a specified threshold value as monazite to produce a binary image. In cases where monazite crystals were touching, we either "separated" them by drawing a line between them before making measurements, or we removed the measurement of the composite grain from our list of measurements. For every crystal, we measured area, perimeter, Feret diameter, and maximum and minimum diameters. For FQMZ series experiments, we made measurements using the Image Processing Toolkit (plug-in tools, which are published by Reindeer Software, for Adobe's Photoshop program), and for MG series experiments SPSS Sigmascan Pro with replicate measurements made using the Image Processing Toolkit.

Crystal-size measurements

Investigators have employed different measures of crystal size in CSD studies: Cashman (1990) advocated measurement of the crystal width or shortest dimension, Higgins (1998) the intermediate dimension, and Peterson (1996) the length or longest dimension. Monazite crystals in our run products are roughly circular in section, and therefore are usually close to spherical in shape. For example, monazite in the run products of FQMZ no. 6 has a mean aspect ratio (= length/width) of 1.5 and a mean shape factor (= 1 for a circle, 0 for a line) of 0.81. The difference in long and short dimensions is small {average % difference = 100 * [(length – width)/length] = 34%}, so it makes little difference which dimension we employ.

TABLE 1. Experimental conditions and measured crystal-size parameters

Expt.	Composition	*t* = duration (h)	*N*	Mag.*	Area (μm^2)	N_A (μm^{-2})	$A_A = V_V$	Shape factor	<*D*>† (μm)	*L*3 (global) (μm)	<*L*>† (μm)	95% C.L.‡
MG no. 0	M + Q§	0	408	1000	4.80E+04	8.50E-03			0.79		0.89	0.07
MG no. 8	M + Q + H_2O	24	1314	1000	1.06E+05	1.24E-02		0.88	0.66		0.74	0.03
MG no. 4	M + Q + H_2O	72	845	1000	9.61E+04	8.79E-03		0.90	0.91		1.04	0.06
MG no. 6	M + Q + H_2O	168	864	1000	1.06E+05	8.15E-03		0.90	1.05		1.2	0.06
MG no. 13	M + Q	24	679	1000	4.63E+04	1.47E-02	0.38	0.91	0.40	0.24 (0.03)	0.48	0.02
MG no. 9	M + Q	72	830	1000	1.06E+05	7.83E-03			0.85		0.97	0.04
MG no. 15	M + Q + H_2O	24	1650	1000	1.89E+05	8.73E-03	1.2	0.84	0.83	0.58 (0.10)	0.90	0.03
MG no. 8-2	M + Q + H_2O	24	1837	1000	1.89E+05	9.72E-03	1.4	0.80	0.84	0.58 (0.12)	0.87	0.03
FQMZ SM	M+Q	0	365	2000	7.17E+04	5.09E-03		0.81	0.48	0.32 (0.08)	0.50	0.04
FQMZ no. 7	M + Q + H_2O	8	294	4000	4.93E+03	5.96E-02	1.16	0.83	0.30	0.29 (0.09)	0.32	0.05
FQMZ no. 5	M + Q + H_2O	37.1	166	4000	1.14E+04	1.46E-02	0.99	0.76	0.50	0.47 (0.14)	0.51	0.1
FQMZ no. 6	M + Q + H_2O	72	245	4000	1.21E+04	2.02E-02	1.48	0.81	0.63	0.51 (0.22)	0.66	0.08

* Magnification of all images of sample taken in back-scattered mode on SEM. Spatial resolution = 0.11 μm/pixel at 1000×, 0.028 mm/pixel at 4000×.

† L represents the diameter of a sphere with the same intercept length as the measured object; *D* is the Feret diameter, the diameter of a circle with the same area as the two-dimensional object. Because measured values of *L* and *D* are log-normally distributed except in the upper and lower tails, we calculated 95% trimmed means of the $\log_{10}$ transformed values and took the antilog to obtain the geometric means of <*L*> and <*D*>, our best estimates of the corresponding population means.

‡ 95% confidence limit on estimate of mean value of *L*, e.g., for MG no.0 there is a 95% probability that the population mean of L falls within the range 0.89 ± 0.07 mm.

§ M = monazite, Q = quartz. Quartz in MG series experiments coarsely crushed and unsieved. Hydrous experiments contained 1–2 wt% H_2O.

We estimated crystal diameters using two methods that yielded similar results. The Feret diameter D is the diameter of a circle having the same area as the object measured, effectively an average diameter. We measured D of every monazite crystal contained in the BSE images of the planar sections of our run products. A stereological measurement technique more commonly employed in CSD studies is to overlay randomly oriented test lines (or a grid pattern on a sample in which the phase of interest is randomly distributed) and measure the number of crystal edge intersections per unit length of test line N_L and the fraction of total test line length that falls within the phase of interest L_L (Russ 1990). These parameters yield the mean intercept length L_3 that is directly related to surface area per unit volume S_V: $L_3 = L_L/N_L = 4V_V/S_V = 4/(S/V)_{\text{mean}}$, where V_V is the volume of crystal per unit volume (volume fraction or modal abundance). The parameter L_3 is a global parameter in that it is a mean value obtained from a random sample of crystals exposed in the planar image. To obtain the distribution of crystal sizes, we measured area and perimeter and calculated L_3 for every crystal contained in the image. Substituting $V_V = A_A$ and $S_V = (4/\pi)B_A$, where B is the total length of boundary line and A is the total area of the image, we obtained $L_3 = 4V_V/S_V = \pi A_A/B_A$. For an individual crystal, B is equal to the perimeter P, and since A_A and B_A are measured on (normalized to) the same area, for an individual crystal $L_3 = \pi A/P$. For a spherical crystal $L_3 = 4V/S = 4(4/3\pi r^3)/4\pi r^2 = 4r/3 = 2L/3$, where L is the diameter of the sphere. Since L_3 also equals $\pi A/P$, we measured A and P for each crystal and calculated the diameter of a sphere $L = 3L_3/2 = 6V_V/S_V = 3\pi A/2P$. We refer to L as the mean intercept length of a crystal, and <*L*> as the mean intercept length of a population of crystals. Values of <*L*> and D were close in value (Table 1) and produced nearly identical histograms, CSD values, and growth curves. Furthermore, values of <*L*> and <*D*> are similar to L_3 measured on multiple images using the line intercept method (Table 1).

Histograms of monazite in starting materials and run products have lognormal distributions (Figs. 3 and 4), so histograms of log (L) are normally distributed. Because parametric statistics require normally distributed data, the antilog of the mean value of log (L) (the geometric mean) provides the best estimate of the population mean <*L*>. However, the log (L) distribution deviates significantly from a normal distribution in the upper and lower tails of the distribution, where we made the smallest number of measurements and errors are greatest. Thus, the most robust estimate of population mean is obtained by calculating the 95% trimmed mean of log (L) by deleting the extreme values in the uppermost and lowermost 5% of the distribution, calculating the mean of log (L), and taking the antilog. Table 1 lists mean values of <*L*> and <*D*> obtained in this way for starting materials and run products along with 95% confidence limits.

Because measured histograms are generally lognormal, estimates of <*L*> and D depend on the spatial resolution and therefore the magnification of the images. Images taken at higher magnification allow measurement of smaller crystals, so estimates of mean crystal size should decrease with increasing magnification. To test this, we measured <*L*> in the run products of MG no. 13 from images taken at 1000× and 2000×. <*L*> estimated from the 1000× images was 0.48 ± 0.02 μm and from 2000× images 0.32 ± 0.02 μm. As a result, we made all measurements in a series at the same magnification (1000× for MG, 4000× for FQMZ except FQMZ SM imaged at 2000×, see Table 1).

Reproducibility

Reliable comparison of grain sizes measured in the products of multiple experiments requires that both the experimental and measurement methods be precise, i.e., reproducible. Experiment MG no. 15 is a replicate of MG no. 8: all experimental methods were the same, but it was imaged on a newer SEM, and image analysis was performed by a different operator using a different program than used for MG no. 8. As seen in Table 1, the results are significantly different: <*L*> = 0.90 ± 0.03 μm for MG no. 15, 0.74 ± 0.03 μm for MG no. 8. We repeated the measurements on MG no. 8 using the same measurement methods used for MG no. 15 and obtained very similar results (MG nos. 8–2 in Table 1; <*L*> = 0.87 ± 0.03 μm; agreement is even closer for D and

L_3). Thus, we can reliably compare measurements from different experiments only if both the experiment and measurement methods are the same, which was the case for all experiments within the MG and FQMZ series.

Measurement of CSD values

Measurements of crystal size made from two-dimensional sections are plotted as histograms of number of crystals per unit area N_A and the cumulative number of crystals per unit area $N*_A$ as functions of L (e.g., Figs. 2, 3, and 4). To allow conversion of these measured 2D parameters to the corresponding 3D parameters N_V and $N*_V$, Peterson (1996) obtained an empirical relationship between $N*_V(L)$ and $N*_A(L)$ by digitally sectioning at random a volume containing crystals of known size distribution, measuring $N*_A(L)$, and adjusting parameters in the following equation to obtain a good fit between known $N*_V(L)$ and measured $N*_A(L)$: $\ln N*_V(L) = \ln (N*_A(L)/[L*S]) + \ln (\gamma) - \beta/[L*S]$, where parameters S (scale) and γ correct the measured lengths and are functions of crystal shape, and the shape factor β depends on the spatial orientation of the crystals. For spheres $S = 1.269$, $\gamma = 0.833$ and $\beta = 0.524$. We used this equation to estimate values of $N*_V(L)$ from measured $N*_A(L)$.

A simple relationship $N*v = N*_{v,0}e^{-L/Gt}$ usually describes cumulative size distributions, where G is the linear growth rate and t is the duration of annealing, and $N*_{v,0} = Gtn_0$, where n_0 is the population density at $L = 0$ (the nucleation density) (Cashman and Ferry 1988). For the population density n defined as the slope of the cumulative frequency curve $-dN*V/dL$, an analogous relationship holds: $n = n_o e^{-L/Gt}$ and $\ln(n) = \ln(n_o) - L/Gt$. Plotting $\ln(n)$ vs. L yields a straight line with slope $= -1/Gt$ and intercept $\ln(n_0)$. Because we know the annealing time in experiments, we can estimate the linear growth rate G from the slope. Peterson (1996, Appendix II) describes the procedures used to estimate n_0 and Gt.

Estimation of coarsening parameters

It has been observed empirically that crystals in dense polycrystalline solids grow at a rate according to $<L>^n - <L>_0^n = K_n t$, where $<L>$ is the mean crystal diameter, n is an integer between 2–4 and K_n is the growth rate constant. It follows that $<L> - <L>_0 = K_{1/n}\ t^{1/n}$, where $K_n = (K_{1/n})^n$ and $K_{1/n}$ has units of $\mu m/s^{1/n}$ (Joesten 1991). Taking logs, $\log <L> = \log <L>_0 + \log K_{1/n} + 1/n \log t$. Plotting $\log <L>$ vs. $\log t$ yields a straight line with slope $1/n$. According to LSW theory, which strictly applies to dispersed phases only, the rate of Ostwald ripening is interface controlled (rate-limited by dissolution or precipitation on the crystal surface) if $n = 2$. This is a typical parabolic rate law in which the rate of growth is proportional to $t^{1/2}$ (Rahaman 1995). If the rate of growth is limited by matrix volume diffusion then $n = 3$, and by grain boundary diffusion then $n = 4$ (Joesten 1991). Calculated values of n range between 2 and 4 and are usually closest to 3, suggesting that matrix diffusion usually limits Ostwald ripening (Rahaman 1995).

After obtaining the value of n from linear regression and rounding to the nearest integer value, we can estimate $K_{1/n}$. If $<L>_0 = 0$, then $L^n = K_n t$, and $\log <L>^n = \log K_n + \log t$. Plotting $\log <L>^n$ vs. $\log t$ and forcing the slope of the best-fit line to equal one yields an intercept of $\log K_n$, from which we obtain K_n and the best estimate of $K_{1/n} = K_n^{1/n}$ (Joesten 1991).

RESULTS

In most experiments 1–2 wt% H_2O was added to increase the rates of recrystallization and growth and therefore speed the approach to textural equilibrium. Discussions below refer to results of hydrous experiments unless stated otherwise.

Textural development

Run products from hydrous MG series matrix coarsening experiments show substantial textural development with time. Run products from anhydrous experiments display crystal shapes and size distributions that are nearly indistinguishable from those in the starting material (Fig. 5a). In contrast, run products from a hydrous experiment of the same duration (Fig. 5b) have larger, less-angular quartz crystals with partially healed fractures. Monazite crystals are present on grain boundaries and commonly occur in clusters. After 72 h (Fig. 5c) quartz crystals have coarsened considerably, in the process occluding many monazite crystals to form arrays of monazite inclusions that are interpreted to represent the original locations of quartz grain boundaries. Quartz crystals also lack angular fracture surfaces or internal fractures, which appear to have healed. These trends in textural development continue in the 168 h run products, which in addition show evidence of progressive growth of monazite crystals present on grain boundaries (Fig. 5d). Many monazite crystals are dumbbell-shaped, having grain boundary outlines that pinch or neck out in the middle of the grain (Figs. 5c and 5e). The shapes appear to represent grain growth by coalescence, a process in which two or more adjacent crystals weld together to form one large composite grain.

In MG series experiments, a large range of quartz crystal size in the starting material (Fig. 2b) resulted in a high rate of quartz coarsening. This in turn led to the development of monazite inclusions, presumably because the low aqueous solubility of monazite at these conditions (0.14 wt%, see Ayers and Watson 1991) prevented monazite crystals from recrystallizing fast enough to maintain their positions on moving quartz grain boundaries. To measure the true growth rate of monazite by Ostwald ripening in quartzite, i.e., the rate of growth of monazite crystals present on grain boundaries and not as inclusions, we took two steps to prevent the occlusion of monazite by quartz crystals (FQMZ experiments). First, we reduced the rate of quartz growth and quartz grain boundary mobility by sieving the quartz to obtain a starting material of uniform crystal size. Second, we used quartz crystals closer in size to the monazite crystals in the starting material (0.45 ± 0.02 μm, Fig. 2a). These steps resulted in run products with near equilibrium textures, containing monazite crystals present almost exclusively on grain boundaries (Figs. 5e and 5f). Pores and monazite crystals preferentially moved to grain triple-junctions and the angle between dry quartz grain boundaries at grain triple-junctions is ~120 °, suggesting a close approach to textural equilibrium (see Watson et al. 1989).

In both sets of experiments dry grain edges and large pores with convex shapes (Fig. 5f) suggest that fluid was non-wetting, and therefore that the dihedral angle θ is >60°. This is consistent

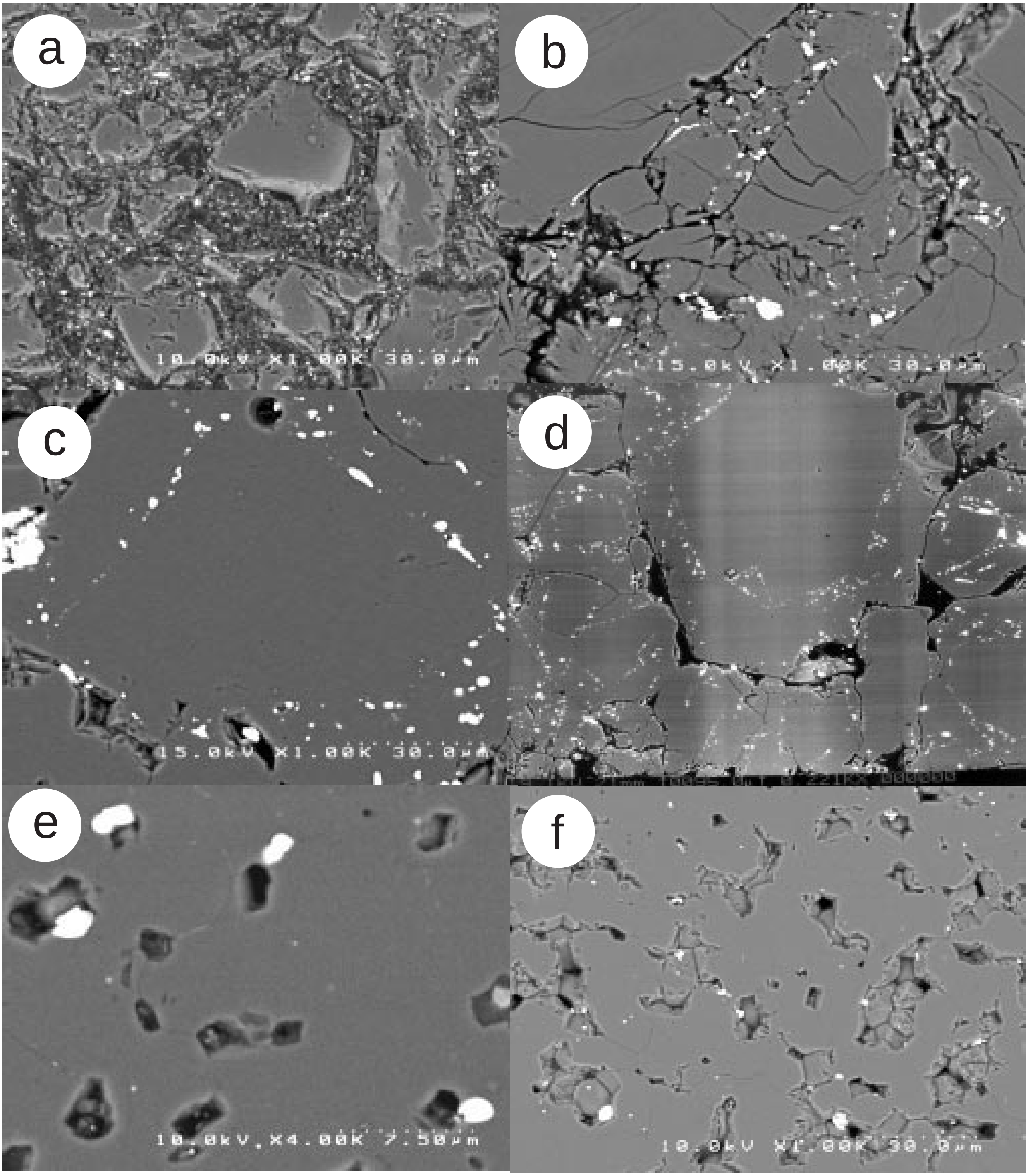

FIGURE 5. BSE images of run products, with magnifications and scale bars. Monazite crystals are white, quartz crystals gray, and pores dark gray-black. (**a**) MG no. 13, anhydrous, 24 h, 1000×. Quartz crystals show no evidence of recrystallization or growth in the run products of this anhydrous experiment. (**b**) MG no. 8, hydrous, 24 h, 990×. Monazite crystals still predominantly on grain boundaries, many in the process of coalescing. Quartz crystals are still heavily fractured from grinding in a mortar and pestle, suggesting that 24 h is insufficient time to anneal out the fractures. (**c**) MG no. 4, hydrous, 72 h, 1000×. Monazite crystals predominantly present as inclusions that form arrays marking the original quartz grain boundary. The direction and extent of quartz crystal growth can be ascertained. (**d**) MG no. 6, hydrous, 168 h, 220×. Large quartz crystals contain numerous monazite inclusions that qualitatively appear to increase in size from core to rim. (**e**) FQMZ no. 5, hydrous, 37.1 h, 4000×. Monazite crystals within or adjacent to pores. The two grains with pinched-in outlines (necking) are crystals in the process of coalescing. (**f**) FQMZ no. 6, hydrous, 72 h, 1000×. Near-equilibrium microtexture: large pores at triple-grain junctions, monazite crystals on grain boundaries and within or adjacent to pores. Dry grain edges and quartz-fluid-quartz dihedral angles >60 ° indicate that the fluid is non-wetting.

with the measurements of Holness (1993), who found that θ = 72 ° at 1000 °C and 0.96 GPa. Thus, fluid was not interconnected at run conditions, and the quartzite was effectively impermeable. However, our results suggest that although the fluid was not interconnected, it greatly affected textural development.

Monazite crystals in our run products show no evidence of internal zoning. This may result from several factors, including that monazite in our starting material was chemically homogeneous (unzoned); that solubility of all components in the fluid was low and fractionation slight or insignificant; and that recrystallization induced by matrix coarsening homogenized the compositions of the monazite crystals.

Crystal-size frequency histograms

As shown in Figure 3a, the distribution of measured diameters of monazite in FQMZ starting material is approximately lognormal, with mean crystal diameter <*L*> = 0.50 ± 0.04 μm (95% confidence limits). After annealing with 2 wt% H_2O at 1000 °C and 1.0 GPa for 8 h, the shape of the histogram is closer to a true lognormal distribution, and <*L*> decreases to 0.32 ± 0.05 μm (Fig. 3b). These observations suggest that during this eight-hour period, original monazite crystals dissolved and new crystals nucleated, producing a lognormal histogram characteristic of recrystallization. After 37.1 h the histogram is more spread out, perhaps by dissolution of smaller crystals and corresponding growth of larger ones, increasing <*L*> to 0.51 ± 0.10 μm (Fig. 3c). After 72 h the trend in shape modification continues, moving closer to a normal distribution and increasing <*L*> to 0.66 ± 0.08 μm (Fig. 3d).

Presumably only monazite present on grain boundaries will grow, either by coalescence or by Ostwald ripening. Thus, measuring the size of monazite crystals present only on grain boundaries as a function of time as in the FQMZ experiments allowed us to accurately estimate the growth rate of monazite. However, in the run products of MG experiment, a large fraction of monazite crystals were present as inclusions, and because grain boundaries intersecting the polished surface at low angles are difficult to detect, we were unable to distinguish inclusions from monazite crystals present on grain boundaries consistently. We were therefore forced to measure the sizes of all monazite crystals, including those present as inclusions, so our measured growth rates in MG series experiments should represent minimum estimates of the true growth rate. Furthermore, since two growth mechanisms (coalescence and Ostwald ripening) operate simultaneously, the measured growth rate equals the sum of the rates of these two processes.

The histogram for the starting material for the MG series experiments (Fig. 4a) has a distribution closer to normal (with positive skewness) than lognormal, with <*L*> = 0.89 ± 0.07 μm. After 24 h the distribution is closer to lognormal, and<*L*> decreases to 0.74 ± 0.03 μm (Fig. 4b), suggesting that as in the FQMZ experiments, monazite partially or completely recrystallized. <*L*> increased to 1.04 ± 0.06 μm after 72 h (Fig. 4c), and 1.20 ± 0.06 μm after 168 h (Fig. 4d), with little change in the shape of the histogram except a subtle decrease in the small size fraction and corresponding increase in the large size fraction indicative of coarsening.

We conducted two anhydrous experiments to quantify the effect of fluid. <*L*> measured from the run products of a 72 h experiment (MG no. 9) is 0.97 ± 0.04 μm, surprisingly close to the value of 1.04 ± 0.06 μm measured in the 72 h hydrous experiment (MG no. 4). However, inspection of the texture of MG no. 9 revealed many features that look like pores, suggesting that our experiment was not truly anhydrous. We therefore took precautions to ensure that our 24 h experiment was anhydrous. First we fired crushable alumina assembly parts at 1000 °C overnight and dried all other assembly parts at 110 °C overnight to remove all adsorbed H_2O. We used an unfired Ni capsule without a Pt insert, reasoning that at the oxidizing conditions of our sample assembly (f_{O_2} between NNO and HM, see Ayers et al. 1992), oxidation of Ni would consume any H_2O contained in the sample to form NiO. Comparison of run product textures (Fig. 5a) with textures of the starting material suggests that no significant textural modification occurred, although <*L*> decreased to 0.48 ± 0.02 μm (Fig. 4e). In contrast, run products from hydrous experiments show evidence of pervasive growth of both quartz and monazite and development of near-equilibrium textures (Fig. 5f). We conclude that the rates of monazite growth and textural development are significantly higher in the presence of fluid.

In both series of hydrous experiments the mean monazite diameters in the shortest duration experiments (Figs. 3b and 4b) were less than in the starting material (Figs. 3a and 4a). The initial size decrease could not have been caused by progressive dissolution in monazite-undersaturated fluid because the fluid could dissolve only ~0.2 wt% of the monazite at saturation (only 1–2 wt% fluid in capsules, solubility of monazite only ~0.14 wt%, see Ayers and Watson 1991). We interpret the initial size decrease to result from monazite recrystallization, either in response to early, rapid quartz coarsening or as a mechanism to eliminate lattice strain acquired during prolonged grinding of the starting material. Because recrystallization decreased the mean size of monazite crystals to a low, unknown value, we were forced to assume that the values at $t = 0$, $\langle D\rangle_0$ and $\langle L\rangle_0$, were equal to zero, resulting in a plot of log <*L*> [rather than log ($\langle L\rangle - \langle L\rangle_0$)] and log <*D*> vs. log *t* in Figure 6. The data for each series plot on a straight line, showing that monazite coarsens at a constant rate. Linear regression of <*L*> measured in FQMZ experiments (r = 0.995) yields a slope of 0.33, corresponding to $n = 3$, suggesting that monazite grows by matrix volume diffusion-controlled Ostwald ripening (Table 2). Plotting log $\langle L\rangle^3$ vs. log *t* and forcing the slope = 1 yields a straight line with intercept = log $K_3 = -5.97$ ($r = 0.997$), corresponding to a value for the rate constant $K_{1/3} = 1.02 \times 10^{-2}$ $\mu m/s^3$. Regression of MG data yields a slope of 0.25 corresponding to $n = 4$, suggesting growth by matrix grain boundary diffusion-controlled Ostwald ripening. Plotting log $\langle L\rangle^4$ vs. log *t* and again forcing the slope = 1 yields a straight line with intercept = log $K_4 = -5.42$ ($r = 0.988$), corresponding to $K_{1/4} = 4.41 \times 10^{-2}$ $\mu m/s^4$.

Crystal-size distributions

Figure 7 shows CSD plots of the natural log of population density ln*(n)* vs. *L* for all experimental run products. Except for some size bins of the shortest experiment FQMZ no. 7 (8 h), all run products show an extremely good linear correlation ($r \geq 0.99$)

between $\ln(n)$ and L, suggesting that the growth rate is nearly constant (Higgins 1998). The best-fit lines obtained by least-squares linear regression describe the relationship $\ln(n) = \ln(n_0) - 1/Gt$, which we used to estimate the values of nucleation densities n_0 from the intercept and growth rate G from the slope. Table 3 lists these values, along with parameters derived from them including the mean crystal size $<L> = Gt$, the total number of monazite crystals per unit volume $N_T = n_0Gt$, and the average nucleation rate $J = N_T/t$ (Cashman and Ferry 1988).

We compare the CSD predicted by LSW theory for Ostwald ripening limited by grain boundary diffusion (n = 4) with measured CSD values of the starting material and run products of MG series experiments in Figure 7a. The CSD predicted by LSW theory is not linear because the theoretical histogram for Ostwald ripening is closer to normal than lognormal. We observe a consistent trend with time toward a CSD closer to that predicted by LSW theory, although even the longest experiment does not come close to attaining the theoretical ideal. Between 0 and 24 h nucleation density n_0 greatly increases (Fig. 8a, Table 3), corresponding to a decrease in the value of the intercept in the CSD (Fig. 7), suggesting extensive recrystallization and nucleation of fresh crystals. Also, $<L> = Gt$ decreases and therefore CSD slope = $-1/Gt$ increases (becomes more negative). Between 24 and 72 h, n_0 decreases and Gt increases (Fig. 8a, Table 3). Little change in slope or intercept occurs between 72 and 168 h, suggesting a steady-state condition.

In Figure 7b we compare the CSD predicted by LSW theory for matrix volume diffusion (n = 3) to the measured CSD values of the starting material and run products of the FQMZ experiments. The measured CSD values do not agree well with the theoretical distribution, nor is there a clear trend as observed for the MG series experiments. Furthermore, as the slope and intercept of the CSD values changes with time (Fig. 8b), steady state was not achieved in the FQMZ experiments, perhaps because no experiments were run as long as the longest MG experiment in which steady-state conditions appear to have been achieved.

DISCUSSION

Abundant evidence suggests that monazite partially recrystallizes and coarsens during high-grade metamorphism, resulting in complex zoning of composition and age (Fig. 1). Experiments designed to characterize monazite recrystallization and coarsening in quartzite + H_2O illustrate the many complexities of the growth process. In the MG matrix coarsening experiments, the large dispersion of size of quartz crystals (Fig.

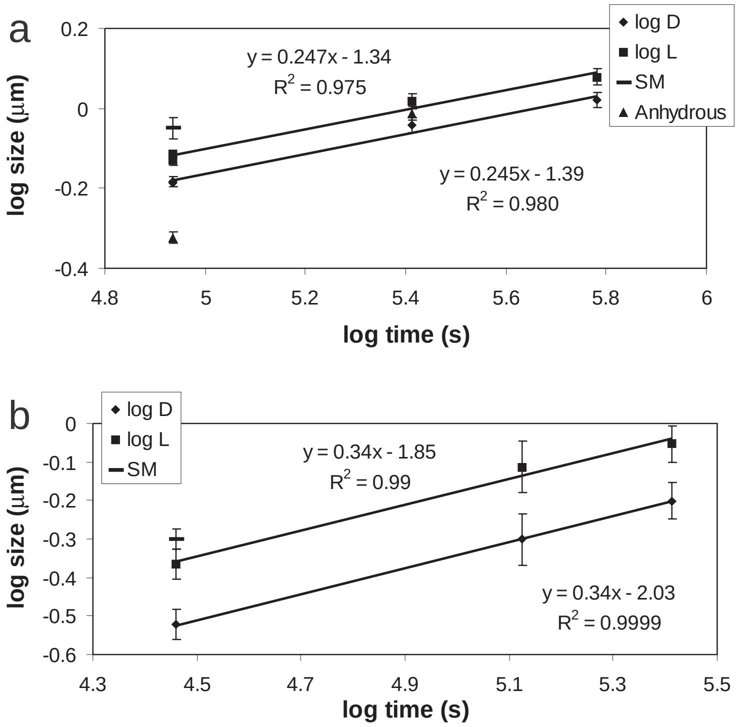

FIGURE 6. Plot of the logarithms of mean intercept length <*L*> (μm) and mean Feret diameter <*D*> vs. $\log_{10}$ time (s). Values of <*L*> and <*D*> represent the 95% trimmed geometric mean for each experiment with 95% confidence limits (see text). Best-fit curves obtained by linear regression shown for hydrous experiments, with corresponding equations and values of correlation coefficient *r*. (**a**) MG series. (**b**) FQMZ series.

TABLE 2. Estimates of *n* and $K_{1/n}$ for monazite growth

Series	1/*n**	Std. Error	*r*	*n*	integer *n*	log K_n†	Std. Error	*r*	$K_{1/n}$ (mm/s$^{1/n}$)
MG	0.247	0.04	0.987	4.05	4	–5.42	0.04	0.988	4.41E-02
FQMZ	0.327	0.024	0.997	3.06	3	–5.97	0.02	0.997	1.02E-02

* 1/*n* equals the value of the slope obtained by least-squares regression of log <*L*> vs. log *t* (see text). Correlation coefficient *r* and standard error on the estimate of the slope also given.

† log K_n equals the value of the intercept obtained by least squares regression of log $<L>^n$ vs. log *t*, where *n* is the integer value of *n* and the slope is constrained to equal one (see text). The correlation coefficient *r* and the standard error on the estimate of the intercept are also given.

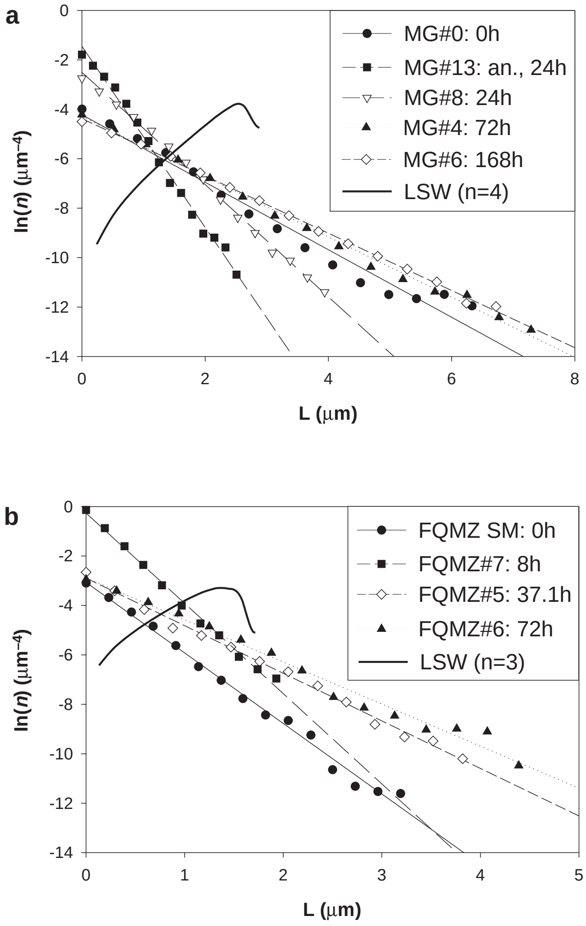

FIGURE 7. CSD plots of the natural log of population density ln(*n*) vs. crystal diameter *L* (µm), calculated using the method of Peterson (1996). The best-fit linear regression curve for each sample is also plotted. (**a**) MG series experiments. The CSD corresponding to the theoretical LSW distribution for *n* = 4 (grain boundary diffusion), calculated using the same size scale as the longest duration experiment MG no. 6, is plotted as a heavy line. (**b**) FQMZ experiments. The CSD corresponding to the theoretical LSW distribution for *n* = 3 (matrix volume diffusion), calculated using the same size scale as the longest duration experiment FQMZ no. 6, is plotted as a heavy line.

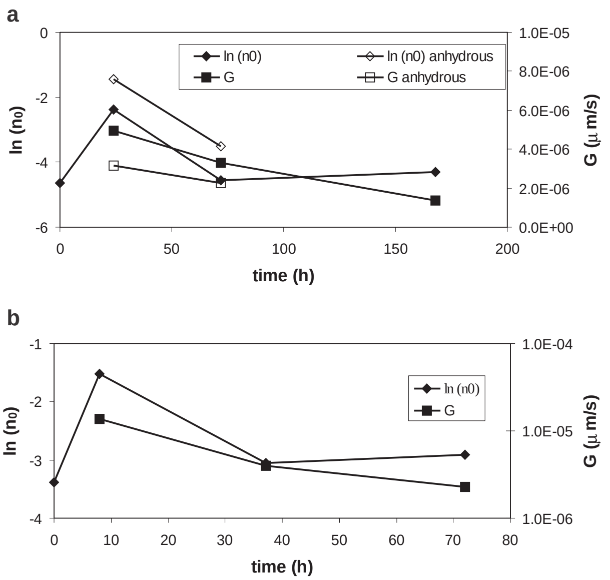

FIGURE 8. Plots of initial nucleation density n_0 and of linear growth rate constant *G* vs. time. (**a**) MG series. (**b**) FQMZ series.

2b) resulted in rapid quartz coarsening and the occlusion of monazite crystals initially present on grain boundaries (Figs. 5c–d). In the FQMZ series experiments containing small quartz crystals of nearly uniform size (Fig. 2a), monazite crystals maintained their position on grain boundaries and grew by Ostwald ripening (Fig. 5e). In both series of experiments monazite also grew by coalescence and a non-wetting fluid phase located primarily in pores at grain triple-junctions promoted the growth of both quartz and monazite. Below we examine these observations in more detail.

Effect of fluid on textural development

Run-product textures show convincingly that fluid was not interconnected at run conditions (e.g., Fig. 5f). However, comparison of run-product textures of anhydrous (Fig. 5a) and hydrous (Fig. 5b) run products from experiments of equal duration (24 h) shows that aqueous fluid strongly affects textural devel-

TABLE 3. CSD Parameters

Expt.	L = Gt (µm)	G (µm/h)	n_0 (1/µm⁴)	r	No. bins	NT = n_0Gt (1/µm³)	J = NT/t (1/µm³h)
MG no. 0	0.79		0.0096	0.9790	14		
MG no. 8	0.43	0.018	0.092	0.9995	14	0.039	0.0016
MG no. 4	0.86	0.012	0.010	0.9980	14	0.0089	0.00012
MG no. 6	0.84	0.005	0.013	0.9995	14	0.011	0.000067
MG no. 13	0.27	0.011	0.235	0.9963	14	0.013	0.00053
MG no. 9	0.58	0.0081	0.030	0.9986	13	0.017	0.00024
MG no. 15	0.62	0.0260	0.022	0.9890	15	0.013	0.00056
MG no. 8-2	0.71	0.0295	0.012	0.9889	15	0.009	0.00035
FQMZ SM	0.38		0.034	0.9919	14		
FQMZ no. 7	0.39	0.049	0.219	0.9800	12	0.086	0.011
FQMZ no. 5	0.53	0.014	0.047	0.9990	13	0.025	0.00067
FQMZ no. 6	0.59	0.0081	0.054	0.9960	14	0.032	0.00044

opment. Most textural development appears to result from growth of quartz by dissolution/reprecipitation that replaces small angular quartz fragments with large rounded or faceted crystals. This process occurs primarily by diffusional transport in pores, where a high aqueous solubility of quartz (18.3 wt% at 1.0 GPa and 1000 °C, see Manning 1994) coupled with a high diffusivity of silica in aqueous fluid assured high diffusive fluxes of silica within pores from small to large quartz crystals. Thus, although the fluid was non-wetting, it greatly increased the rate of quartz coarsening.

The presence of fluid has a smaller influence on monazite crystal size. In the 24 h experiments the difference between mean crystal diameters in hydrous and anhydrous run products is small (0.48 μm in the anhydrous experiment, 0.78 μm in the hydrous experiment). The effect of fluid on monazite growth may be small because the fluid did not form an interconnected network but instead segregated to pores at grain triple-junctions. Furthermore, because the modal abundances of monazite and fluid are low, few monazite crystals may have initially been in contact with fluid. Even when monazite crystals are in contact with fluid, the low aqueous solubility of monazite (Ayers and Watson 1991) translates to low fluxes of monazite components in the fluid. These factors contributed to a relatively low rate of monazite growth in our experiments.

Monazite growth mechanisms

Coarsening of monazite and quartz occurs primarily through a process of dissolution-precipitation in the presence of fluid. The growth of monazite is diffusion-controlled, as shown by the values of *n* obtained from MG experiments ($n = 4$, grain boundary diffusion control) and FQMZ experiments ($n = 3$, volume diffusion control). At ambient conditions, dissolution-precipitation rates of soluble minerals are transport (diffusion) controlled, and rates for insoluble minerals such as monazite are interface controlled (a surface reaction is the rate-limiting step). However, because interface-controlled reactions have higher activation energies than diffusion, the rates of interface-controlled reactions increase faster with increasing *T* (Langmuir 1997). Our results are consistent with the idea that the rates of dissolution and precipitation (growth) of all minerals are transport-controlled at high *T*.

That $<L>$ increases regularly with time (Fig. 6) is strong evidence that Ostwald ripening occurs, because Ostwald ripening decreases the surface area per unit volume $S_V = 6V_V/<L>$, and since V_V is constant, S_V must decrease as $<L>$ increases. That run product CSD values do not resemble steady-state profiles predicted by LSW theory (Fig. 7) does not mean that Ostwald ripening is not an important growth mechanism in our experiments; in fact, given that the modal abundance V_V of monazite is constant, Ostwald ripening is the only potential growth mechanism other than coalescence. Most experimental and field-based studies have produced normalized histograms with wider distributions than predicted by LSW theory (see discussion and references in Cashman and Ferry 1988). This is probably because of the unrealistic assumption of LSW theory that the modal abundance V_V of the dispersed phase is zero (Voorhees 1992). Also, in our experiments matrix coarsening and the resulting recrystallization and coalescence of monazite crystals act to spread out the size distribution and slow the approach to textural equilibrium as defined by LSW theory. Thus, evidence indicates that Ostwald ripening is an important growth mechanism for monazite in our experiments.

However, Ostwald ripening was not the only monazite growth mechanism. During quartz coarsening, monazite crystals migrated with mobile quartz grain boundaries, in many cases encountering other monazite crystals with which they coalesced. Run products from both sets of experiments show clear textural evidence of growth by coalescence, such as necking (Fig. 5e) and irregular composite crystals with multiple branches (Fig. 5b).

Matrix coarsening and inclusion/host relations

Theory and experiment have shown that the most thermodynamically stable position for accessory minerals such as monazite is on grain boundaries (Watson et al. 1989). Monazite crystals present on grain boundaries exert a force on the grain boundary known as “Zener drag” that opposes its movement during matrix coarsening. Large crystals especially will tend to “pin” host grain boundaries, which is why ceramicists often add a dispersed phase (dopant) to limit the growth of crystals during fabrication of ceramics (Rahaman 1995). Thus, conventional wisdom states that accessory minerals pin host grain boundaries during metamorphic coarsening, maintaining their position on grain boundaries and preventing further growth of host crystals (e.g., Watson et al. 1989). This is especially true for large crystals (Bea 1996). However, matrix coarsening is common during metamorphism even when accessory minerals are present. Furthermore, monazite in high-grade metamorphic rocks is typically present as inclusions, especially in biotite (e.g., Bea 1996). Textural relations suggest that monazite crystals in these high-grade metamorphic rocks did not pin grain boundaries, but rather were swallowed up by growing host crystals. When crystals of monazite and other accessory minerals are present as inclusions, they do not control the concentrations of their essential structural constituents during melting or fluid infiltration. Furthermore, monazites present as inclusions are less likely to be altered or experience diffusive Pb loss (Poitrasson et al. 1996), and thus may be more resistant to resetting of the U,Th-Pb system than monazites present on grain boundaries. Thus, it is important to know under what conditions monazite will be present as inclusions or on grain boundaries.

Whether accessory mineral crystals and their host grain boundaries separate or remain attached depends on their relative rates of migration. During matrix coarsening grain boundaries migrate toward their centers of curvature, and accessory mineral crystals migrate with the grain boundaries by fluid-assisted recrystallization. Figure 9 describes the textural development of rocks containing pores or other grain-boundary impurities (Rahaman 1995). The velocities of accessory mineral crystals and host grain boundaries, calculated as functions of the sizes of accessory mineral and host crystals, define three boundary curves along which accessory mineral crystals and host grain boundaries have equal mobilities. In a fluid-bearing rock, the solubilities and diffusivities of dissolved host and accessory mineral components determine the mobilities of ac-

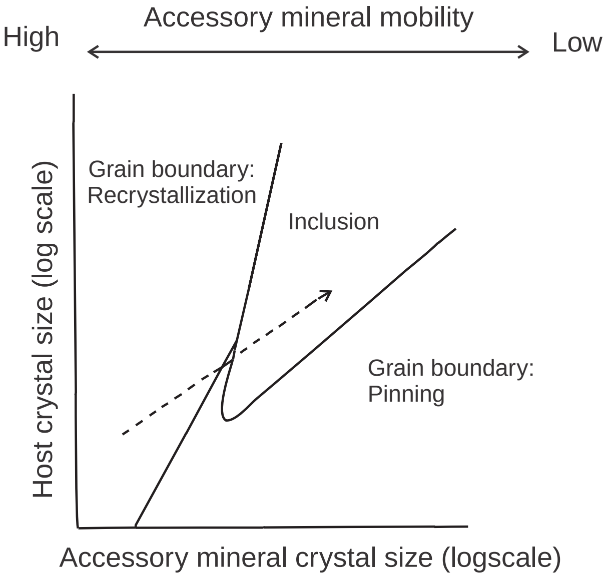

FIGURE 9. Schematic diagram illustrating the effect of host and accessory mineral crystal-size on inclusion-host relations (after Rahaman 1995). The dashed arrow illustrates how coarsening of host quartz and monazite may cause quartz to occlude monazite grains originally on grain boundaries.

cessory mineral crystals and host grain boundaries and therefore the positions of the boundary curves. An accessory mineral has high mobility if it is highly soluble in the fluid and its dissolved components have high aqueous diffusivities.

Accessory mineral crystals can maintain their energetically favorable positions on grain boundaries either by moving faster than a mobile grain boundary or by immobilizing the grain boundary. In the "pinning" field in Figure 9, accessory mineral crystals are large compared with host crystals so that the Zener drag force is large and accessory mineral crystals maintain their positions by pinning grain boundaries. In the "recrystallization" field, accessory mineral crystals are small so they can recrystallize rapidly and maintain their positions on migrating grain boundaries by moving with them. In the "inclusion" field, the accessory mineral crystals are too small to pin grain boundaries and too large to recrystallize rapidly, and their velocities are less than those of the grain boundaries, so the growing host crystals engulf them to form inclusions. We can see from Figure 9 that inclusions are least likely to develop when both host and accessory crystals are small, as in FQMZ experiments. However, the development of inclusions in MG experiments was not only a result of the quartz crystals being on average larger than monazite crystals and larger than quartz crystals in the FQMZ experiments, but also a result of increased grain boundary mobility. Anything that increases the mobility of host grain boundaries promotes the development of inclusions. The rate of matrix coarsening in MG experiments was much higher than in FQMZ experiments due to the larger range of quartz crystal sizes in the MG starting material (compare Figs. 2a and 2b; note that the boundaries in Fig. 9 pertain to accessory mineral and host crystal populations of uniform size). Thus, given a wide range of host crystal sizes as in the MG experiments, the rate of coarsening and the mobility of host grain boundaries will be high, and accessory mineral crystals are more likely to become occluded.

In the MG experiments most monazite crystals were on grain boundaries after 24 h (Fig. 5b), but after 72 h they were present almost exclusively as inclusions (Fig. 5c). This corresponds to the path illustrated by the dashed arrow in Figure 9 in which the starting material plots in the recrystallization field. Quartz and monazite coarsening during the first 24 h shifted the rock microtexture into the inclusion field.

Interestingly, zircon growth experiments identical to the MG series experiments yielded run products in which zircon was predominantly present on grain boundaries (Ayers et al. 1998). We used the same quartz starting material in the two sets of experiments, and the initial mean crystal sizes of zircon and monazite were very similar, yet monazite became occluded while zircon did not. We suspect that zircon crystals were more mobile, and therefore less likely than monazite to be present as inclusions, because zircon has a higher aqueous solubility than monazite at the same conditions (Ayers and Watson 1991).

Measured growth rates and their application

Measured growth constants (Table 2) can be used to estimate the amount of time required to grow grains of specified size or rims of specified thickness. Figure 10 plots $L-L_0$ (μm) vs. time (y) calculated using the growth constants obtained by regression of MG and FQMZ data (Table 2). The y axis represents the diameter of a newly grown monazite crystal ($L_0 = 0$), or twice the thickness of a rim formed on an older core by coarsening. The amount of growth is greater for $n = 4$ than for $n = 3$ up to ~1 y, consistent with our observation that on the timescale of our experiments monazite grew faster in MG than in FQMZ experiments. After 1000 y the mean diameter of monazite crystals in quartzite at 1000 °C should increase 18.6 μm if growth is controlled by grain-boundary diffusion as in MG experiments, and 32.2 μm if controlled by volume diffusion as in FQMZ experiments. The growth parameters can also be used to estimate the duration of metamorphic growth from measured grain size or rim thickness. For example, a monazite crystal with a metamorphic rim = 32.2/2 = 16.1 μm thick could form in 1000 y at 1000 °C. Growth rates are probably lower at lower *T*, and higher if the fluid is interconnected. Monazite growth by Ostwald ripening in the presence of fluid is fast enough to cause significant growth during high-grade metamorphic events, and should produce rims that yield concordant U,Th-Pb dates corresponding to the age of ripening.

Interpretation of CSD values

Our CSD plots (Fig. 7), which are linear over nearly the entire range of measured crystal sizes, are similar to those measured by Cashman and Ferry (1988) in contact metamorphic rocks, but unlike CSD values from regionally metamorphosed rocks that show a peak in the CSD at intermediate size. Cashman and Ferry (1988) attributed the depletion of small crystals of magnetite in regionally metamorphosed rocks to Ostwald ripening during prolonged annealing. In contrast, they found mag-

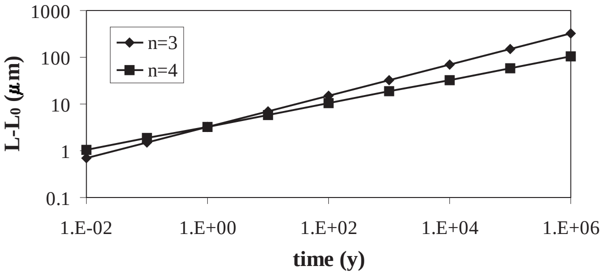

FIGURE 10. Plot of $L–L_0$ (μm) vs. time (y) calculated from $L–L_0 = K_{1/n}t^{1/n}$ using the growth constants obtained by regression of MG and FQMZ data (Table 2). The y axis represents the diameter of a newly grown monazite crystal ($L_0 = 0$), or twice the thickness of a rim formed on an older core by coarsening.

netite in contact metamorphic rocks to have lognormal histograms, and CSD values linear over the entire range of measured crystal sizes. They interpreted the linear CSD values to result from continuous nucleation and growth, with the largest crystals being the oldest and smallest crystals representing freshly nucleated crystals.

For minerals that are solid solutions such as magnetite, continuous nucleation and growth during contact metamorphism may result from new growth (increasing modal abundance) over a range of *T* (because of solid-solution effects in minerals participating in the heterogeneous mineral-forming reaction). However, our assumption has been that the modal amount of monazite is constant. This assumption must be true because the solubility of monazite is negligible in quartz and is only 0.14 wt% in H_2O at these conditions (Ayers and Watson 1991). Since there are roughly equal masses of monazite and H_2O in the starting material, only ~0.14 wt% of the monazite would be dissolved in the fluid at saturation. How can there be continuous nucleation and growth if the modal abundance of monazite is constant?

One possible answer is that monazite recrystallized through most (or all) of the experiment duration. The process that causes extensive recrystallization during the early stages of the experiments must be completed before growth returns $<L>$ to its initial value $<L>_0$ (the mean crystal size in the starting material) between 24 and 37.1 h. This would represent the amount of time it takes the fluid to dissolve and reprecipitate all of the monazite. Simultaneously, quartz coarsening causes continuous recrystallization of monazite, maintaining a constant supply of freshly nucleated crystals as reflected in a lognormal histogram. This process operates concurrently with Ostwald ripening, but it decreases the overall rate of monazite growth (note that Ostwald ripening cannot produce small crystals; it only consumes them). Thus, matrix coarsening-induced recrystallization seems responsible for continuous recrystallization and nucleation over the time span studied, effectively slowing the rate of monazite growth. However, higher growth rates in MG experiments must result from the higher coarsening rate, which increased the rate of coalescence and promoted Ostwald ripening by placing monazite crystals in pores. Since matrix coarsening results in an increase in the net growth rate, the increase in crystal size from coalescence and Ostwald ripening is greater than the decrease resulting from recrystallization. We predict that given more time, monazite growth would produce normally distributed histograms and convex-up CSD values as observed by Cashman and Ferry (1988) in regionally metamorphosed rocks.

Summary and implications for U,Th-Pb dating

Our results show that when fluid is present during high-grade metamorphism, host crystals coarsen by dissolution-reprecipitation, and small accessory mineral crystals either recrystallize and move with host grain boundaries or are engulfed by growing host crystals to form inclusions. Recrystallization of small monazite crystals on grain boundaries during matrix coarsening erases preexisting zoning and resets the U,Th-Pb isotopic systems. Large monazite crystals may immobilize grain boundaries by pinning them. Monazite crystals on immobile grain boundaries may grow by Ostwald ripening to produce rounded crystals with young, chemically homogeneous rims mantling older cores. Analysis of these crystals by TIMS is likely to yield a linear discordia on a concordia diagram. Ages obtained from in-situ analysis of overgrown rims may represent the timing of fluid influx or of growth during peak metamorphism.

Small monazite crystals present on mobile grain boundaries of large host crystals are likely to become inclusions because, due to a low aqueous solubility, they cannot recrystallize fast enough to maintain the more stable grain boundary position. This explains why monazite is commonly present in metamorphic rocks as inclusions (Bea 1996). Included crystals are isolated from further growth and textural development and from the effects of fluid alteration, and therefore are more likely to retain their original U,Th-Pb isotopic signatures. These observations highlight the importance of knowing the textural setting of dated grains, and suggest that combining in-situ textural and dating studies will lead to more accurate interpretations of measured ages.

ACKNOWLEDGMENTS

This paper represents part of the third author's M.S. thesis, and the fourth author's Senior Honor's thesis, both at Vanderbilt University. Funding was provided by NSF grant no. EAR-9506551 and grant no. EAR-9873626 to Ayers and Miller. Tony Peterson provided an Excel spreadsheet for plotting CSD values. Oran Switzer helped develop the image analysis procedures and replicated our measurements. Thanks to Alan Wiseman and Jim Wittig for their assistance on the SEM. Reviews by Fernando Bea and Yuanming Pan helped to improve the manuscript.

REFERENCES CITED

Akers, W.T., Grove, M., Harrison, T.M., and Ryerson, F.J. (1993) The instability of rhabdophane and its unimportance in monazite paragenesis. Chemical Geology, 110, 169–176.

Ayers, J.C. and Watson, E.B. (1991) Solubility of apatite, monazite, zircon and rutile in supercritical aqueous fluids with implications for subduction zone geochemistry. Philosophical Transactions Royal Society London A, 335, 365–375.

Ayers, J.C., Brenan, J.B., Watson, E.B., Wark, D.A., and Minarik, W.G. (1992) A new capsule technique for hydrothermal experiments using the piston cylinder apparatus. American Mineralogist, 77, 1080–1086.

Ayers, J.C., Milleman, J., and Gorisch, E.B. (1998) Experimentally determined inclusion/host relationships in accessory-mineral bearing quartzites at high-grade metamorphic conditions. EOS, 79, S358.

Bea F. (1996) Residence of REE, Y, Th and U in granites and crustal protoliths: Implications for the chemistry of crustal melts. Journal of Petrology, 37, 521–552.

Bingen, B. and van Breeman, O. (1998) U-Pb ages in amphibolite- to granulitefacies orthogneiss reflect hydrous mineral breakdown reactions: Sveconorwegian Province of SW Norway. Contributions to Mineralogy and Petrology, 132, 336–353.

Cashman, K.V. (1990) Textural constraints on the kinetics of crystallization of igneous rocks. In Mineralogical Society of America Reviews in Mineralogy, 24, 259–314.

Cashman, K.V. and Ferry, J.M. (1988) Crystal-size distribution (CSD) in rocks and the kinetics and dynamics of crystallization III. Metamorphic crystallization. Contributions to Mineralogy and Petrology, 99, 401–415.

Deer, W.A., Howie, R.A., and Zussman, J. (1966) An introduction to the rock forming minerals. Longman, 528 p.

Fitzsimmons, I.C.W., Kinny, P.D., and Harley, S.L. (1997) Two stages of zircon and monazite growth in anatectic leucogneiss; SHRIMP constraints on the duration and intensity of Pan-African metamorphsim in Prydz Bay, East Antarctica, Terra Nova, 9, 47–51.

Getty, S.R. and Gromet, L.P. (1992) Geochron-ological constraints on ductile deformation, crustal extension, and doming about a basement-cover boundary, New England Appalachians. American Journal of Science, 292, 359–397.

Gratz, R. and Heinrich, W. (1997) Monazite-xenotime thermobarometry: Experimental calibration of the miscibility gap in the binary system $CePO_4$-YPO_4. American Mineralogist, 82, 772–780.

Hawkins, D.P. and Bowring, S.A. (1997) U-Pb systematics of monazite and xenotime: case studies from the Paleoproterozoic of the Grand Canyon, Arizona. Contributions to Mineralogy and Petrology, 127, 87–103.

Heaman, L. and Parrish, R. (1991) U-Pb geochronology of accessory minerals. In Heaman, L., and Ludden, J.N., Eds., Applications of Radiogenic Isotope Systems to Problems in Geology. Mineralogical Association of Canada Handbook, volume 19, 59–102.

Higgins, M.D. (1998) Origin of anorthosite by textural coarsening: quantitative measurements of a natural sequence of textural development, Journal of Petrology, 39, 1307–1323.

Holness, M.B. (1993) Temperature and pressure dependence of quartz-aqueous fluid dihedral angles: the control of adsorbed H_2O on the permeability of quartzites. Earth and Planetary Science Letters, 117, 363–377.

Joesten, R.L. (1991) Kinetics of coarsening and diffusion-controlled mineral growth. In Mineralogical Society of America Reviews in Mineralogy, 26, 507–582.

Kingsbury, J.A., Miller, C.F., Wooden, J.L., and Harrison, T.M. (1993) Monazite paragenesis and U-Pb systematics in rocks of the eastern Mojave Desert, California: Implications for thermochronometry. Chemical Geology, 110, 147–168.

Langmuir, D. (1997) Aqueous Environmental Geochemistry, 600 p. Prentice Hall, Upper Saddle River, New Jersey.

Lanzirotti, A. and Hanson, G.N. (1996) Geochronology and geochemistry of multiple generations of monazite from the Wepawaug Schist, Connecticut, USA; implications for monazite stability in metamorphic rocks. Contributions to Mineralogy and Petrology, 125, 332–340.

Lifshitz, I.M. and Slyozov, V.V. (1961) The kinetics of precipitation from supersaturated solid solutions. Journal of Physics and Chemicals of Solids, 19, 35–30.

Manning, C.E. (1994) The solubility of quartz in H_2O in the lower crust and upper mantle. Geochimica et Cosmochimica Acta**,** 58, 4831–4840.

Miller, C.F., Gorisch, E.B., Harrison, T.M., Coath, C.D., and Hatcher, R.D. (1996) Elucidating complex crustal histories through combined zoning and high resolution IMP radiometric studies of zircon and monazite: an example from the Blue Ridge, NC-GA. EOS, 77, F819.

Miller, C.F., D’Andrea, J.L., Ayers, J.C., Coath, C.D., and Harrison, T.M. (1997) BSE imaging and ion probe geochronology of zircon and monazite from plutons of the Eldorado and Newberry Mountains, Nevada: age, inheritance, and subsolidus modification. EOS, 78, F783.

Overstreet, W.C. (1967) The geological occurrence of monazite. U.S. Geological Survey Progress Paper 530.

Pan, Y. (1997) Zircon- and monazite-forming metamorphic reactions at Manitouwadge, Ontario. Canadian Mineralogist, 35, 105–118.

Parrish, R.R. (1990) U-Pb dating of monazite and its application to geological problems. Canadian Journal of Earth Science, 27, 1431–1450.

Peterson, T.D. (1996) A refined technique for measuring crystal-size distributions in thin section. Contributions to Mineralogy and Petrology, 124, 395–405.

Poitrasson, F., Chenery, S., and Bland, D.J. (1996) Contrasted monazite hydrothermal alteration mechanisms and their geochemical implications. Earth and Planetary Science Letters, 145, 79–96.

Rahaman, M.N. (1995) Ceramic processing and sintering. Marcel Dekker Inc., New York, N.Y., 770 pp.

Rapp, R.P. and Watson, E.B. (1986) Monazite solubility and dissolution kinetics: Implications for the thorium and light rare earth chemistry of felsic magmas. Contributions to Mineralogy and Petrology, 94, 304–16.

Russ, J.C. (1990) Computer-assisted microscopy. Plenum Press, New York.

Sawka, W.N., Banfield, J.F., and Chappell, B.W. (1986) A weathering related origin of widespread monazite in S-type granites. Geochimica et Cosmochimica Acta, 50, 171–175.

Smith, H.A. and Barreiro, B. (1990) Monazite U-Pb dating of staurolite grade metamorphism in pelitic schists. Contributions to Mineralogy and Petrology, 105, 602–15.

Suzuki, K., Adachi, M., and Kajizuka, I. (1994) Electron microprobe observations of Pb diffus- ion in metamorphosed detrital monazites. Earth and Planetary Science Letters, 128, 391–405.

Townsend, K.J., Miller, C.F., D’Andrea, J.L., Ayers, J.C., Harrison, T.M., and Coath, C.D. (1998) Monazite replacement during modification of the Ireteba granite, southern Nevada: Geochronological implications. GSA Abstracts with Programs, 30, A214.

Voorhees, P.W. (1992) Ostwald ripening of two-phase mixtures. Annual Reviews Material Science, 22, 197–215.

Wagner, C. (1961) Theorie den Alterung von Nieder schlaegen durch Umloesen (Ostward Reifung). Zeitschr. Elektrochemie, 65, 581–591.

Watson, E.B., Vicenzi, E.P., and Rapp, R.P. (1989) Inclusion/host relations involving accessory minerals in high-grade metamorphic and anatectic rocks. Contributions to Mineralogy and Petrology, 101, 220–231.

MANUSCRIPT RECEIVED NOVEMBER 10, 1998
MANUSCRIPT ACCEPTED JULY 7, 1999
PAPER HANDLED BY PHILIP PICCOLI